materials

Article

An Easy and Ecological Method of Obtaining Hydrated and Non-Crystalline WO_{3-x} for Application in Supercapacitors

Mariusz Szkoda [1,*], Zuzanna Zarach [1], Konrad Trzciński [1], Grzegorz Trykowski [2] and Andrzej P. Nowak [1]

[1] Department of Chemistry and Technology of Functional Materials, Faculty of Chemistry, Gdańsk University of Technology, Narutowicza 11/12, 80-233 Gdańsk, Poland; zuziaz696@gmail.com (Z.Z.); trzcinskikonrad@gmail.com (K.T.); andnowak@pg.edu.pl (A.P.N.)
[2] Faculty of Chemistry, Nicolaus Copernicus University in Toruń, Gagarina 7, 87-100 Toruń, Poland; tryki@umk.pl
* Correspondence: mariusz.szkoda@pg.edu.pl

Received: 22 March 2020; Accepted: 16 April 2020; Published: 19 April 2020

Abstract: In this work, we report the synthesis of hydrated and non-crystalline WO_3 flakes (WO_{3-x}) via an environmentally friendly and facile water-based strategy. This method is described, in the literature, as exfoliation, however, based on the results obtained, we cannot say unequivocally that we have obtained an exfoliated material. Nevertheless, the proposed modification procedure clearly affects the morphology of WO_3 and leads to loss of crystallinity of the material. TEM techniques confirmed that the process leads to the formation of WO_3 flakes of a few nanometers in thickness. X-ray diffractograms affirmed the poor crystallinity of the flakes, while spectroscopic methods showed that the materials after exfoliation were abundant with the surface groups. The thin film of hydrated and non-crystalline WO_3 exhibits a seven times higher specific capacitance (C_s) in an aqueous electrolyte than bulk WO_3 and shows an outstanding long-term cycling stability with a capacitance retention of 92% after 1000 chronopotentiometric cycles in the three-electrode system. In the two-electrode system, hydrated WO_{3-x} shows a C_s of 122 F g^{-1} at a current density of 0.5 A g^{-1}. The developed supercapacitor shows an energy density of 60 $Whkg^{-1}$ and power density of 803 Wkg^{-1} with a decrease of 16% in C_{sp} after 10,000 cycles. On the other hand, WO_{3-x} is characterized by inferior properties as an anode material in lithium-ion batteries compared to bulk WO_3. Lithium ions intercalate into a WO_3 crystal framework and occupy trigonal cavity sites during the electrochemical polarization. If there is no regular layer structure, as in the case of the hydrated and non-crystalline WO_3, the insertion of lithium ions between WO_3 layers is not possible. Thus, in the case of a non-aqueous electrolyte, the specific capacity of the hydrated and non-crystalline WO_3 electrode material is much lower in comparison with the specific capacity of the bulk WO_3-based anode material.

Keywords: exfoliation; hydrated non-crystalline WO_3; supercapacitors; lithium-ion batteries; anode material

1. Introduction

The increase in global energy consumption, caused by the rapid increase in population, forces the production of energy storage and energy conversion systems on a larger scale. However, the utilization of fossil fuels has led to changes in the Earth's climate by increased emissions of greenhouse gases [1]. Thus, new energy sources are expected to meet the requirements of being renewable and emission-free [2]. To meet these expectations, more and more attention is being paid to energy storage devices such as supercapacitors and batteries. Supercapacitors may store electrical energy of a high power density but low energy density without any conversion reactions [3]. Batteries require an electrochemical reaction to obtain electrical energy from a chemical reaction in a reversible way [4], assuming a high energy density. Despite the various energy storage mechanisms, one can assume that transition metal oxides may be successfully adapted as electrode materials for supercapacitors as well as for batteries (for example, Co_3O_4, MnO_x, TiO_2) [5–7]. This is due to the fact that properties of metal oxides are strongly dependent on many factors, i.e., crystal structure, morphology, doping and oxygen deficiency [8]. One of the methods of some transition metal oxides' modification is exfoliation, which leads to the formation of 2D flakes.

The amusing physical and structural properties of atomically thin 2D materials are the result of their improved surface-to-volume ratio, altered surface energy and the confinement effect [9,10]. Throughout recent years, rapid progress has been achieved in establishing procedures of graphene preparation [11] and transition metal dichalcogenides in the form of single or few layers [12–14], as a consequence of the slow breakdown of van der Waals force between the adjacent layers in bulk. Nevertheless, the family of 2D materials is being expanded, especially by transition metal oxides, in order to greatly develop their progressive applications [15].

Among many transition metal oxides, tungsten (VI) oxide (WO_3) is attracting much attention. It has been used in electrochromic devices [16], gas sensors [17], electrocatalysis [18] and photoelectrocatalytic processes [19]. Recently, many studies have shown that WO_3 may be utilized as an energy storage material [20–22]. Lokhande et al. evidenced that the crystal structure affects the energy storage ability of WO_3-based electrode materials [23]. There are many factors of synthesis that have an influence on the crystallographic structure, morphology and properties of obtained materials, i.e., temperature, pH, pressure, the time, the presence of additives, etc. [24–27]. Exfoliation is one of the modification methods to obtain 2D nanomaterials from layered materials [28] and is expected to improve electrodes' performance in terms of both stability and capacity [29]. Apart from tungsten oxide, there is a major number of other metal oxides that were reported to enhance working properties of the energy storage devices. Ruthenium oxide is widely investigated because of its high specific capacitance (up to 700 F/g), but its application is severely limited by the high cost [30]. Metal oxides such as MnO_2 [31] or NiO [32] have similar advantages and there have been some attempts to apply them as electrode materials. However, their poor electrical conductivity affects the speed of charging and contributes to severe capacitance loss. To improve the capacitive performance of materials with a poor electrical conductivity, many researchers found oxygen-defective metal oxides to be of the greatest interest. Reported results show that the concentration of oxygen vacancies has a significant influence on the structure, as well as charge storage properties, and thus enable an excellent cycling performance [33–36].

Several approaches are accessible for the manufacture of WO_3 2D materials, including hydrothermal, solvothermal, plasma treatment, acid etching, anodization and exfoliation. Over the last decade, many methods for the exfoliation of layered materials have been investigated for the synthesis of monolayer nanostructures. Mechanical exfoliation was firstly applied by Geim and Novoselov [37] to obtain graphene by using adhesive tapes. Nevertheless, it is difficult to obtain uniform samples by this technique. The other one, and one of the most commonly used techniques, is liquid exfoliation that could be combined with oxidation or ion intercalation/exchange, as well as surface passivation by solvents [10]. In the case of metal oxides, the exfoliation usually involves sonication in a surfactant solution and ion or polymer intercalation [38–40]. The application of the latter method leads to obtaining single layers in a crystalline form, possessing the promising properties and gives large quantities of a dispersed nanomaterial. However, amorphous materials also find various applications, yet they are still gaining less interest. To our knowledge, most of the research in which amorphous materials of a nanometric scale were obtained are limited in zero-dimensional (0D) and one-dimensional (1D), like amorphous MoO_{3-x} nanoparticles or amorphous $FeCoPO_x$ nanowires [41–45]. All of the above-mentioned showed excellent activity in catalysis and local surface plasmon resonances (LSPR). However, there are still many attempts to obtain 2D materials, especially with confined thickness, that would have the superior activity and the ability of application in many fields. One of the latest studies, provided by Ren et al. [46], suggested using the supercritical CO_2 technology to obtain the two-dimensional amorphous heterostructures of Ag/a-WO_{3-x} and proposed the concept of synergistic photocatalysis, which would serve as a new methodology for the design of a high-efficiency catalyst.

In this work, we used a process to modify the material, which is described in the literature as exfoliation. However, based on the results obtained, we cannot say unequivocally that we have obtained an exfoliated material. Nevertheless, we received a material characterized by non-crystallinity and the surface was enriched with the surface groups. Hence, this paper outlines the influence of a facile water-based strategy and its effect on the structure, morphology and electrochemical properties of WO_3. It is evidenced that this strategy may improve the electrode's performance for a supercapacitor application but it is not convenient for energy storage via a faradaic reaction in batteries.

Even if, for instance, the exfoliation process, proposed in the literature and used by us, leads to obtaining an exfoliated material, the presence of obtained structures would, in this work, result from the method of electrode preparation that consists of the slow evaporation of water which may partially reverse the exfoliation effect. Nevertheless, the proposed modification procedure clearly affects the morphology of WO_3 and leads to the loss of crystallinity of the material.

2. Materials and Methods

2.1. Synthesis of Hydrated and Non-Crystalline WO_3 and Electrodes Preparation

Bulk WO_3 (Sigma, analytical grade, Saint Louis, MI, USA) was added, as received, to triple-distilled water to create a suspension with a concentration of 60 mg mL^{-1} and was refluxed for 10 days at 80 °C. The suspension obtained after 10 days was transparent and bulk WO_3 residues could not be distinguished. Very often centrifugation is necessary to separate larger, non-exfoliated crystallites. In the case of this developed procedure, the step of centrifugation can be omitted because under the proposed conditions, the process occurs with almost 100% efficiency. The solid residues were not present in the exfoliated solution, as it is presented in Figure 1. The exfoliation of WO_3 occurs readily, even under dark conditions (via covering the reaction vessel with aluminum foil), which reveals that the visible light does not play a significant role in the exfoliation process. In this paper, hydrated and non-crystalline WO_3 was synthesized via refluxing under natural light.

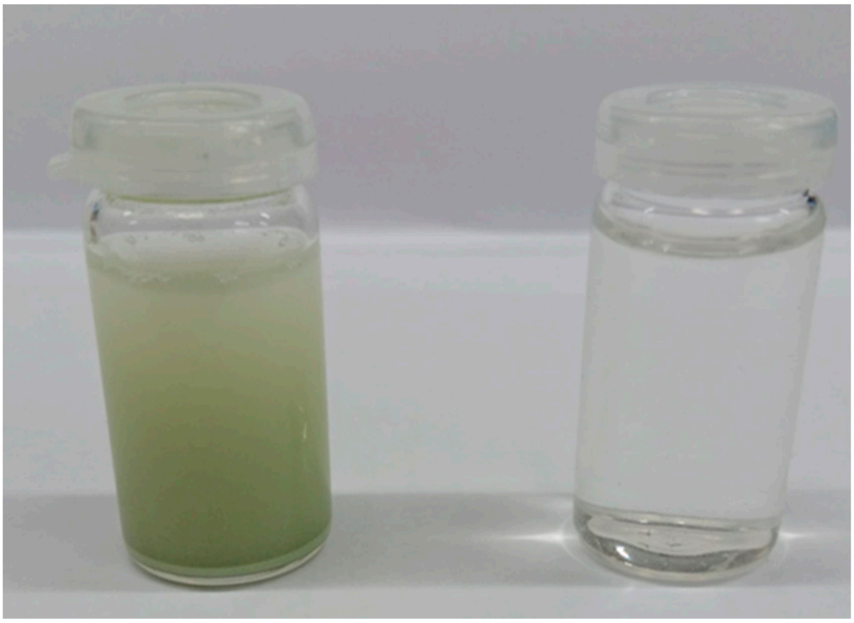

Figure 1. The photographs of WO_3 suspensions before (left) and after (right) the exfoliation process.

In the case of the modified WO_3, the working electrodes for the electrochemical measurements in an aqueous electrolyte were prepared by a drop-casting method. The volume of 200 µL of an aqueous suspension of the WO_{3-x} was drop-casted onto the ~0.67 cm^2 degreased FTO (fluorine-doped tin oxide) glass (Sigma, 7 Ω/sq, Saint Louis, MI, USA). The mass loading of the electrode material after water evaporation at 80 °C ranged from 5.6 to 8.2 mg cm^{-2}. WO_3 bulk powder was deposited onto the FTO glass using the dip-coating method. At first, 0.2 g of material and about 0.1 g of poly(ethylene oxide-PEO) (M = 300,000, Aldrich) were mixed with 1 ml of water in order to obtain a homogenous mixture. The degreased FTO was immersed in the WO_3/PEO/H_2O, pulled out, dried, and heated for 5 h at 400 °C in an air atmosphere. The thermal treatment led to the PEO (poly(ethylene oxide)) removal from the deposited film. The procedure of solid material deposition on the substrate was previously elaborated [47]. In this case, the mass of the WO_3 layer loading ranged from 7.2 to 11 mg cm^{-2}.

The suspension concentration of the hydrated WO_{3-x} was transferred to the Petri dish. The excess of water was slowly evaporated at 45 °C. The obtained yellow powder of WO_{3-x} nanoflakes was dried at 80 °C for 24 h and was used for the material characterization (TEM, SEM, XRD, XPS, FTiR), as well as for the electrode preparation for the electrochemical measurements performed in a non-aqueous electrolyte. Battery tests were performed with electrodes obtained from a slurry containing WO_3 (bulk or modified), carbon black (CB) (Super P, Timcal, Bodio, Switzerland), and pVDF (Polyvinylidene fluoride, Solvay) at a weight ratio 7:2:1 dissolved in NMP (N-methyl-2-pyrrolidinone, AlfaAesar) on a copper current collector (Schlenk Metallfolien GmbH & Co KG, Georgensgmünd, Germany). The discs of 10 mm were cut off, pressed for 30 s under a 2 MPa load, and finally dried for 24 h at 100 °C under a dynamic vacuum in an oven (Glass Oven B-595, Büchi, Germany). The mass loading of the electrode material was around 3 mg cm^{-2}.

2.1.1. Morphology and Crystal Structure

The morphology was examined using scanning electron microscopy (Quanta 3D FEG, Fei Company), with the beam accelerating voltage kept at 20 kV, and transmission electron microscopy (Tecnai 20F X-Twin, Fei Company, Cambridge, UK). The preparation of the samples for the TEM imaging consisted of sonication for 5 s of a few milligrams of bulk or modified WO_3 in ethanol (99.8% anhydrous) using ultrasounds, and then an applied drop (5 µL) on a carbon-coated copper mesh with holes (Lacey type Cu 400 mesh, Plano), and the evaporation of the solvent was at a room temperature. The crystal structure of the prepared materials was studied with powder X-ray diffraction (XRD). Patterns were obtained by an X'Pert Pro diffractometer with an X'Celerator detector and Cu Kα radiation, $\lambda = 0.15406$ nm. The infrared spectra (FTiR) in the 300–4000 cm^{-1} range were recorded in a vacuum spectrometer Vertex 70V, Bruker Optic, with a T = 22 °C, $p = 10^{-1}$ Pa, resolution of 4 cm^{-1}, and a number of 50 scans. The sample was mixed with KBr at a mass ratio of 1/300, then compressed at 7 MPa to form a pellet, and then the transmission spectrum was recorded. The chemical composition measurements for the material after the exfoliation process were performed by the X-ray photoemission spectroscopy method. The XPS measurements were performed using an Argus Omicron NanoTechnology X-ray photoelectron spectrometer.

2.1.2. Electrochemical Measurements

Aqueous electrolyte: The electrochemical measurements were performed in a 0.2 M K_2SO_4 aqueous electrolyte purged with argon. A three-electrode cell was used for the cyclic voltammetry and galvanostatic charge–discharge cycles measurements. A platinum mesh acted as a counter electrode and Ag/AgCl (3 M KCl) was used as the reference electrode. The electrochemical studies were conducted using the AutoLab PGStat204 potentiostat-galvanostat system (Methrom, AutoLab, Utrecht, The Netherlands). The charge–discharge measurements were carried out with a current density equal to 0.2 A g^{-1} in a polarization range from −0.15 to 0.9 V vs. Ag/AgCl (3 M KCl). The galvanostatic charge–discharge measurements for the hydrated WO_{3-x} were also performed using fully assembled symmetric two-electrode cells in a coffee bag system. The commercially available foil was used for the preparation of the supercapacitor cells. A Whatman paper was used as a separator. An aqueous solution of 0.2 M K_2SO_4 was used as an electrolyte. Coffee bags were enclosed under a vacuum using a Mini Jumbo Henkelman Vacuum System. The supercapacitor cells were tested using multiple galvanostatic charge–discharge cycles (10,000 cycles, $j_c = j_a = 0.5$ A g^{-1}).

The electrochemical impedance spectra (EIS) for both electrode materials were recorded using AutoLab PGStat10 for the working electrode at its rest potential and under anodic polarization. The frequency range covered 10 kHz–0.32 Hz (90 points), whereas the amplitude of the AC signal equaled 10 mV. The following elements were used for the fitting procedure of the measured impedance spectra using EIS Analyzer software: *R*: resistance, *CPE*: constant phase element, and Z_{Wo}: finite length diffusion impedance, where:

$$Z_{W_o}(\omega) = \frac{W_{or}}{\sqrt{\omega}}(1 - j)\coth\left(W_{oc}\sqrt{j\omega}\right) \tag{1}$$

$$Z_{CPE}(\omega) = P^{-1}(j\omega)^{-n} \tag{2}$$

Non-aqueous electrolyte: The electrode materials were tested in two-electrode Swagelok® cell with lithium foil (99.9%, 0.75 mm thickness, AlfaAesar, Haverhill, MA, USA) as a counter and a reference electrode. The SelectiLyte™ LP30 (1 M LiPF6 in EC/DMC 50:50, wt %) from Merck was used as an electrolyte and a glass fiber (Schleicher & Schüll, city, Germany) as a separator. The battery tests of the samples were performed using the ATLAS 0961 MBI (ATLAS_SOLLICH, Banino Poland) multichannel battery testing system at current densities of 50 mA g^{-1}, from 0.01 V to 3 V. The cyclic voltammetry measurements (CV) were carried out on a PGStat204 galvanostat/potentiostat over the potential range from 0.005 V to 3V vs. Li/Li^+, with a scanning rate of 0.1 mV s^{-1}.

3. Results and Discussion

3.1. Morphology and Structure

The morphology of the WO_3 samples was tested using the SEM technique. The micrographs of the bulk WO_3 are presented in Figure 2a,b. As can be seen, the non-modified powder is built of grains of various sizes in the order of several dozen micrometers. Regular shapes and sharp edges are distinctive for a crystalline material. Higher magnification reveals a layered structure of the bulk WO_3 (see Figure 2b). The material after modification is characterized by a different morphology, as is shown in Figure 2c. Slowly-dried, hydrated WO_{3-x} forms agglomerates with irregular shapes. They are clearly different to the crystallites of the bulk WO_3. Aggregates of an exfoliated WO_3 are built of randomly oriented plates of heterogeneous shapes with a size of 0.7–1.5 µm (see Figure 2d and inset Figure 2d). The thicknesses of the flakes were roughly estimated to be in the order of 50–100 nm (see Figure S1 in Supplementary Information). The presence of such thick structures results from the method of sample preparation that consists of the slow evaporation of water which may partially reverse the exfoliation effect. Thus, the proposed modification procedure clearly affects the morphology of WO_3 and leads to the delamination of the material. However, a better insight into the morphology of the material was obtained using TEM. As is shown in Figure 3, the appropriate sample preparation for the TEM imaging allows ultra-thin nanoflakes of WO_{3-x} to be observed. The transparency of the layers under TEM reveals that the thickness should not exceed a few nanometers.

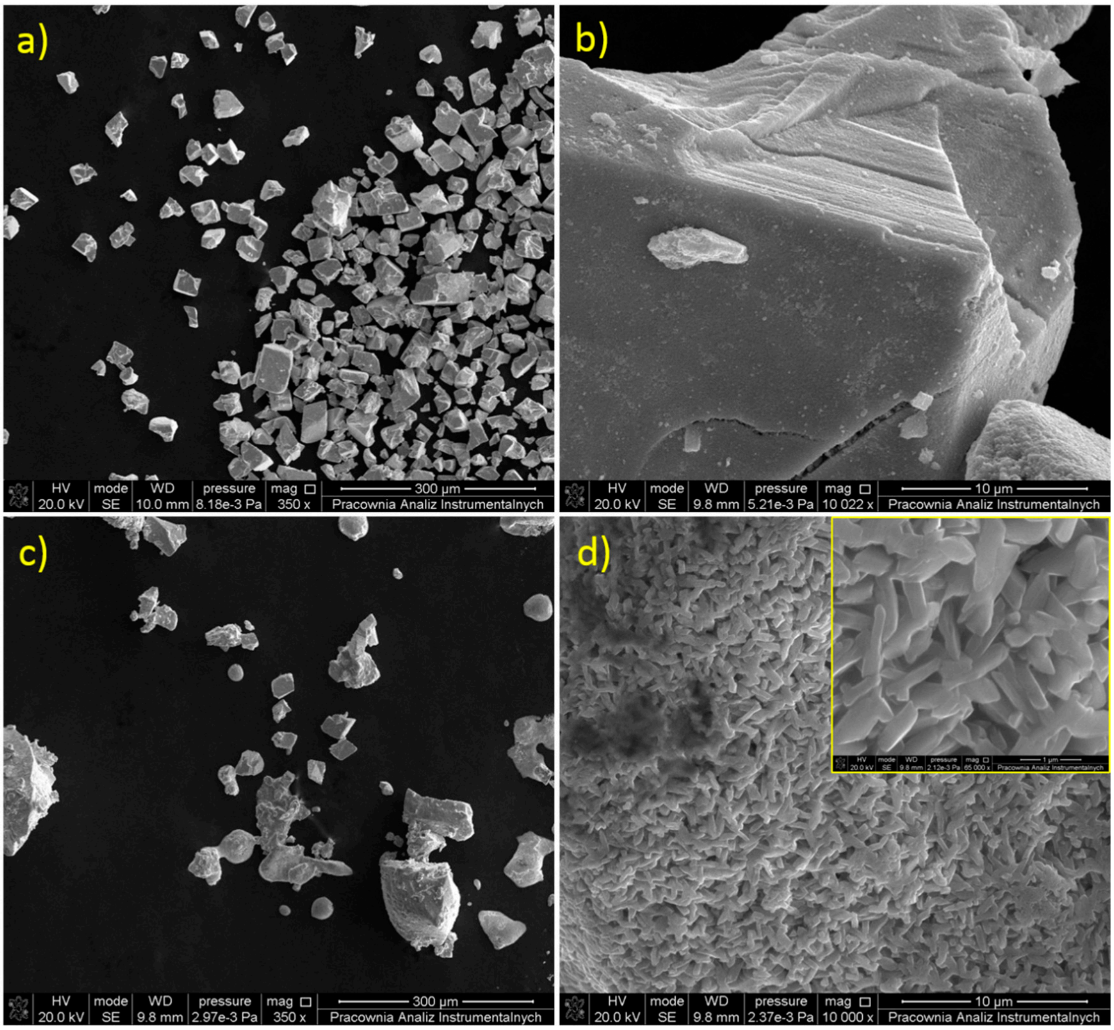

Figure 2. SEM images of (**a**,**b**) bulk and (**c**,**d**) hydrated and non-crystalline WO_3.

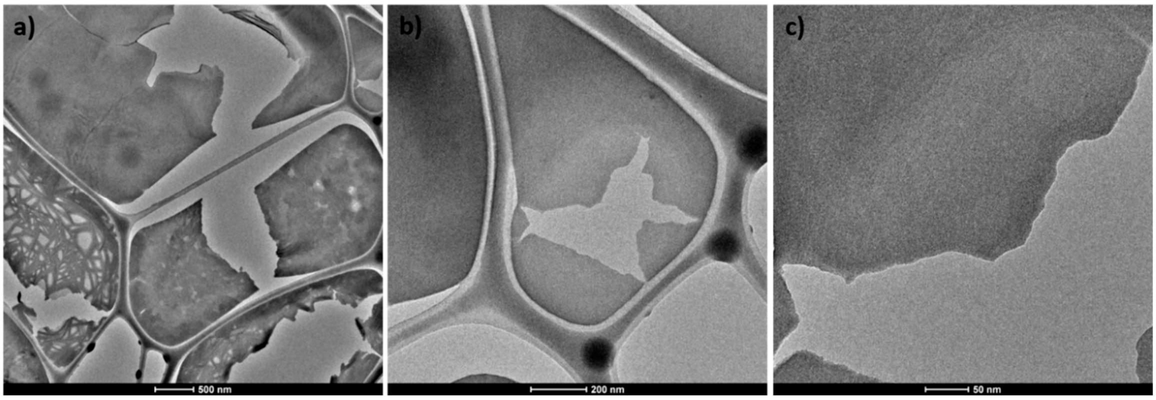

Figure 3. (**a**–**c**) TEM images of hydrated and non-crystalline WO_{3-x}. at various magnifications.

FTIR spectroscopy was used to analyze the functional groups of the bulk WO_3 and WO_3 after modification. As can be seen in Figure 4, the two spectra are different from each other in the range 600–1000 cm^{-1}. In the case of the modified WO_3, peaks are observed at 780, 890 and 940 cm^{-1}. These bands can be attributed to the O-W-O vibrations, while the band at 1630 cm^{-1} is linked to the bending modes of the O–H groups. The W-O stretching modes are less intense, and changes in the low-frequency modes may indicate some modifications in the tungsten oxide framework. The appearance of the most active surface centers suggests a connection with defects in the nanoflakes [48]. The non-crystalline WO_3 sample has a large number of defects that somehow activate W-O vibrations in the range 600–1000 cm^{-1}. This phenomenon is missing in the bulk sample, which is why the W-O vibrations are inactive, and thus not visible in the FTIR spectrum are peaks at 780, 890 and 940 cm^{-1}. A similar effect was observed on the pristine Zn-Al and exfoliated samples [49]. Another band at 3430 cm^{-1} is linked to the stretching modes of the OH groups in water or hydroxyls [50]. On the basis of relative intensities, it can be concluded that there are many more OH groups in the modified sample. It can also be indicated by the widening of the peak at 3400 cm^{-1}, that can be divided into two bands at approximately 3430 and 3100 cm^{-1}. Both bands are assigned to the OH group, however, they differ chemically. The OH group at 3430 cm^{-1} is connected to the adsorbed water, and the OH group at 3100 cm^{-1} is directly bound to the WO_3 structure.

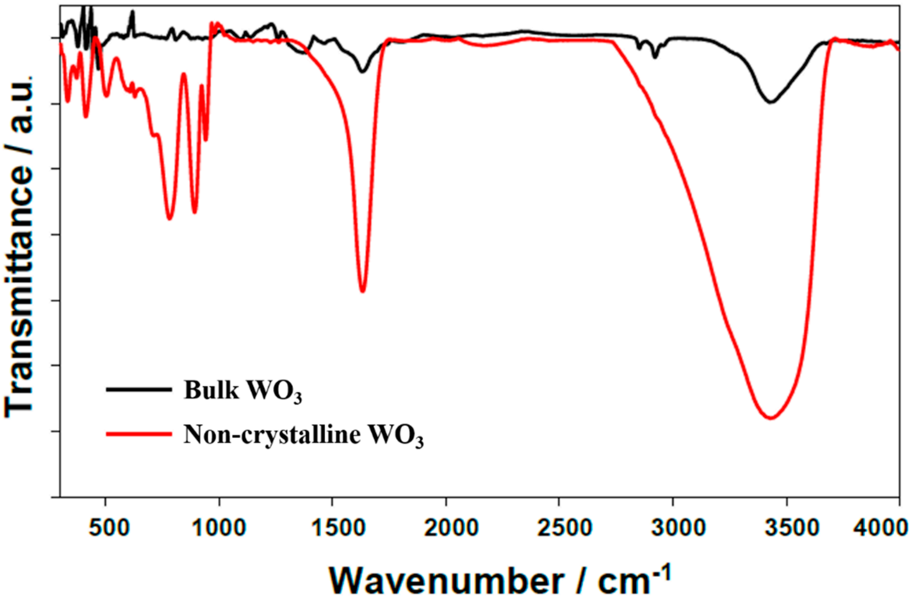

Figure 4. FTIR spectra of bulk and hydrated and non-crystalline WO_3.

The crystal structures of the samples were examined by the powder X-ray diffraction technique (Figure 5). In the case of the bulk WO_3, all the reflexes could be assigned to the monoclinic phase of WO_3. No other reflexes were detected, confirming phase purity. As is shown in Figure 5a, the amorphous structure was detected for the WO_{3-x} nanoflakes, suggesting the lack of crystallinity. Poor crystallinity in the exfoliated transition metal oxide (MoO_{3-x}) was also observed by Ahmed S. Etman et al. [51]. Nevertheless, low-intensity peaks can be found (see Figure 5b). However, these signals do not come from the crystalline form of WO_3. On the basis of the XRD pattern, it can be concluded that hydrated WO_3 is composed of an amorphous phase, but both orthorhombic tungsten trioxide hydrate (o-$WO_3 \cdot H_2O$) and hexagonal tungsten oxide hydrate (h-$WO_3 \cdot 0.33H_2O$) traces can be detected [52].

Due to the fact that the obtained result in the form of the hydrated and non-crystalline material was unexpected after applying the exfoliation technique, it is difficult to make a comparison as most of the exfoliation results provide a crystalline phase of the material. What is more, the process of the exfoliation of transition metal oxides, a tungsten oxide in particular, is not as widely studied as, for example, the process of graphene exfoliation. However, there are individual studies on this topic. In both Kalantar-Zadeh et al.'s [53] and Yan et al.'s [54] works, they used hydrated WO_3 as the precursor, which is a typical layered material consisting of planes connected through the interaction of oxygen and hydrogen through hydrogen bonds in the adjacent layers. Waller et al. [55] exfoliated $Bi_2W_2O_9$, and in each of these researches, the crystalline phase of the final product was obtained. By comparing the results presented in Table 1, it can be stated that regardless of which exfoliation technique was used, tungsten oxide was obtained in a crystalline form. In the case of the nanoflakes obtained during the experiment presented in this work, the exfoliated product might have undergone hydration, which has determined its final properties. The use of the water exfoliation technique may also be related to obtaining poor crystallinity. Similar results were obtained by Etman et al. [51], who also observed poor crystallinity for the MoO_3 nanosheets, also utilizing a water-based exfoliation.

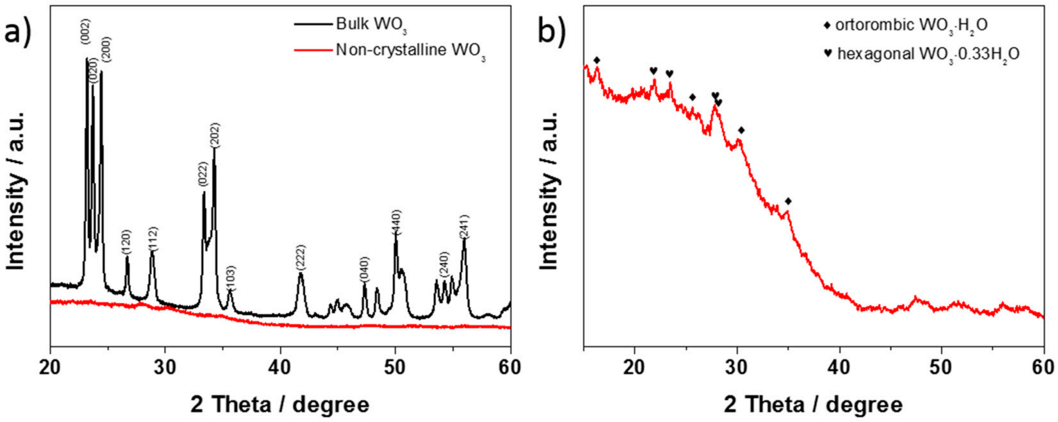

Figure 5. XRD patterns of (**a**) bulk and hydrated and non-crystalline WO_3, (**b**) only hydrated and non-crystalline WO_3.

Table 1. Methods and characteristics of the exfoliation process.

Material	Method	Precursor	Solvent	Layer Thickness	Crystalline Phase	Ref.
WO_3 Nanosheets	Mechanical exfoliation	$WO_3 \cdot 2H_2O$	-	1.4–100	m-WO_3	[53]
WO_3 Nanosheets	Alcohothermal exfoliation	$WO_3 \cdot nH_2O$	Absolute ethanol	8–20	m-WO_3	[54]
Nano-WO_3	Chemical exfoliation	$Bi_2W_2O_9$	Concentrated hydrochloric acid; tetramethylammonium hydroxide solution	0.75	$WO_3 \cdot 0.5H_2O$	[55]
WO_3 Nanosheets	Electrostatic-driven exfoliation	WO_3 powder	BSA solution (pH 6-4)	1.4; 2.1	m-WO_3	[56]
$WO_3 \cdot 2H_2O$ Nanosheets	Ultrasonic exfoliation (intercalation with dodecylamine)	H_2WO_4	Concentrated nitric acid solution	1.4	$WO_3 \cdot 2H_2O$	[57]
WO_3 Nanoflakes	Water exfoliation	Bulk WO_3	Water	60–80	Amorphous	This work

X-ray photoelectron spectroscopy (XPS) analysis was employed to investigate the oxidation states and the presence of oxygen vacancies in the hydrated and non-crystalline WO_3. The high-resolution XPS spectra for the tungsten and oxygen region are presented in Figure 6. The W 4f core-level XPS spectrum can be deconvoluted into four peaks corresponding to the W^{6+} and W^{5+} states (see Figure 6a). The peaks located at the binding energies of 35.83 and 37.97 eV correspond to the W^{6+} state, while the peaks at 34.96 and 37.11 eV correspond to W^{5+}. The splitting between W 4f7/2 and W 4f5/2 for the W^{6+} state is 2.13 eV, which is in good agreement with an earlier report [58]. The emergence of the W^{5+} oxidation state can be associated with the presence of oxygen vacancies that are formed during exfoliation. Therefore, the chemical structure can be referred to as WO_{3-x}.

The O 1s spectrum shows a broad asymmetric peak, which can be deconvoluted into three peaks, as shown in Figure 6b. The main peak (red curve) at 530.4 eV is assigned to the oxygen atoms (O^{2-}) that form the strong W = O bonds [59,60]. This value is slightly lower than that reported for the commercial powder WO_3 (531 eV) [61], suggesting a change in the coordination environment between the O and W atoms in the exfoliated WO_3. The peak at 531.6 eV (blue curve) can be assigned to the surface-adsorbed species (OH^-, O^-, or oxygen vacancies) [62,63]. Finally, the peak at 533.4 eV (green curve) can be assigned to adsorbed water [63], proving the existence of $WO_3(H_2O)_n$ phases at the surface [64].

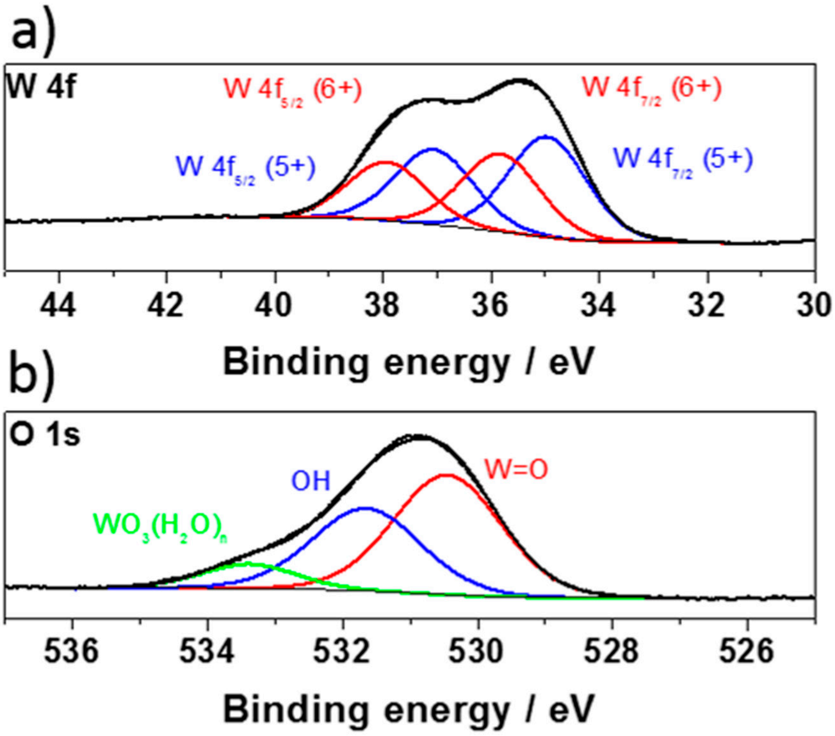

Figure 6. XPS spectra of (**a**) W 4f and (**b**) O 1S core levels of hydrated WO_{3-x}.

3.2. *Electrochemical Properties*

3.2.1. Aqueous Electrolyte

Three-Electrode System Configuration

Electrochemical studies of the modified WO_3 electrodes were carried out in order to evaluate their utility as an electrode material for supercapacitors. The CV (cyclic voltammetry) curves recorded for the bulk and modified electrode materials are presented in Figure 7a. The measurements were carried out in the potential range of −0.15 to +0.9 V vs. Ag/AgCl/3M KCl, with a scan rate equal to 50 mV s^{-1}. The hydrated WO_{3-x} material displays a highly rectangular shape without redox peaks, which indicates a capacitive nature of the electrode material. Cyclic voltammetry results show a good charge–discharge reversibility of the electrode process. The current plateau characteristic for electrical double layer capacitance (EDLC) was recorded. The EDL activity observed at a wide range of applied potential may be related to the presence of a high concentration of oxygen vacancies and OH surface groups, whose presence was confirmed using XPS and IR techniques. It was previously reported that WO_3-based supercapacitors exhibited both pseudocapacitance and EDLC. However, the contribution of pseudocapacitance was much higher [20]. In the case of the hydrated WO_{3-x}, the electrode material characterized by a specific morphology as well as having a surface enriched in surface groups, it may be expected that the contribution of EDLC is significantly higher in comparison with the bulk WO_3. The contribution of pseudocapacitance is also expected, however, the lack of clear oxidation/reduction peaks on the CVs may be related to the lack of the hydrated WO_{3-x}crystallinity. As can be seen, the bulk WO_3 exhibited decidedly lower current densities compared with the non-crystalline WO_3 nanoflakes. The CV curve of the bulk WO_3, in contrast to the modified material, exhibits oxidation/reduction peaks that were observed previously and described as the conversion of the valence states of W centers with simultaneous adsorption/desorption of cations available in the electrolyte [65].

The CVs of the hydrated WO_{3-x} recorded at different scan rates (5–500 mV s^{-1}) are presented in Figure S2. The anodic current density at 0.5 V shows a linear relation with the scan rate (see Figure S2b), suggesting that the charge storage is controlled by the surface processes, thus it is not a diffusion-controlled phenomenon (see Figure S2c).

Both electrode materials were compared using electrochemical impedance spectroscopy. Two spectra for each type of electrode were registered (Figure S4). The first one was recorded close to the rest potential (0 V vs. Ag/AgCl (3 M KCl), and the second under anodic polarization (0.6 V vs. Ag/AgCl (3 M KCl). The results, equivalent circuits, and fitting parameters are presented in the supplementary information (see Figure S3 and Table S1). The EIS analysis confirms that the diffusion process affects the impedance spectrum only of the bulk WO_3 recorded at 0 V, seen as a straight line inclined at an angle of 45° at the lowest frequencies, and the Warburg element (W_o) is necessary to fit the model properly. In the case of a hydrated WO_{3-x} model, it can be fitted using a simpler equivalent circuit, without the W_o. The comparison of the fitting parameters of the bulk and hydrated tungsten oxide electrodes recorded under anodic polarization confirms that hydrated WO_{3-x} can act as an electrode material for energy storage devices, mainly supercapacitors.

Multiple galvanostatic charge–discharge tests were carried out for both electrodes in a 0.2 M K_2SO_4 aqueous electrolyte (Figure 7b). The polarization with an anodic and cathodic current gives almost identical capacitance values, indicating a reversible process with over 99% of columbic efficiency (Figure 7c). The electrode that contains the non-crystalline WO_3 exhibits a seven times higher specific capacitance than the bulk WO_3 due to the higher surface area of the interface between the electrode material and the electrolyte, and a higher concentration of W-OH surface groups that participate in the charge storage process. After a sequence of 1000 charge–discharge cycles, over 92% and 80% of the initial capacitances were maintained for the non-crystalline and bulk WO_3, respectively. In the case of the bulk WO_3, the capacitance retention after 1000 cycles was lower compared with the modified material. It may be related to the fact that the capacitance of the bulk WO_3 mainly comes from the W centers reduction/oxidation and ions' intercalation/deintercalation, while a modified material utilizes a highly reversible electroactivity of the surface groups.

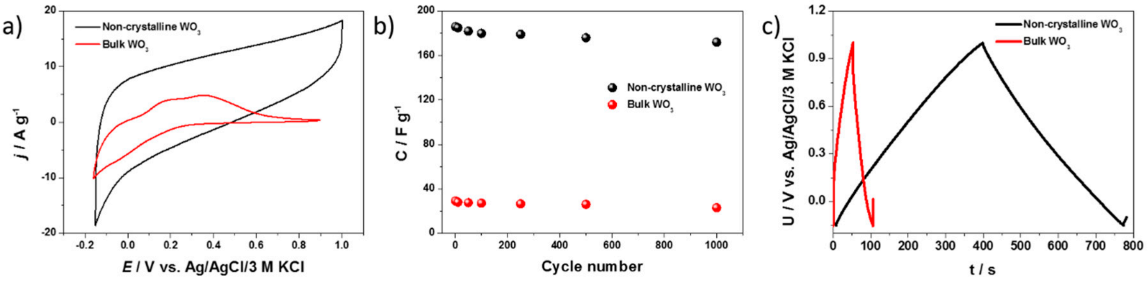

Figure 7. (**a**) Cyclic voltammograms for the non-crystalline and bulk WO_3. (**b**) Curves of specific capacitance vs. cycle number for hydrated and bulk WO_3. (**c**) Exemplary galvanostatic charge–discharge curves of electrodes at 0.2 A g^{-1} (in a three-electrode configuration).

Two-Electrode Configuration

Multiple charge–discharge cycles in a two-electrode configuration for the hydrated WO_{3-x} were performed in order to test the stability of the tested supercapacitor (see Figure 8). As is shown, a very good stability, even after 10,000 cycles, was obtained for the hydrated WO_{3-x}-based capacitor. The capacitance retention between the 1st and the 10,000th chronopotentiometry cycle was equal to 84%. The effect of the capacitance drop was also tracked using chronopotentiometry. The curves recorded before and after a long-term test are presented also in the Figure 8 inset. It is noteworthy that the decrease of the capacitance is the highest at the beginning of the charge–discharge tests, and then the capacitance stabilized after approximately 2000 cycles. This means that the capacitance drop is not related to the electrolyte decomposition, but some irreversible reactions on the material surface.

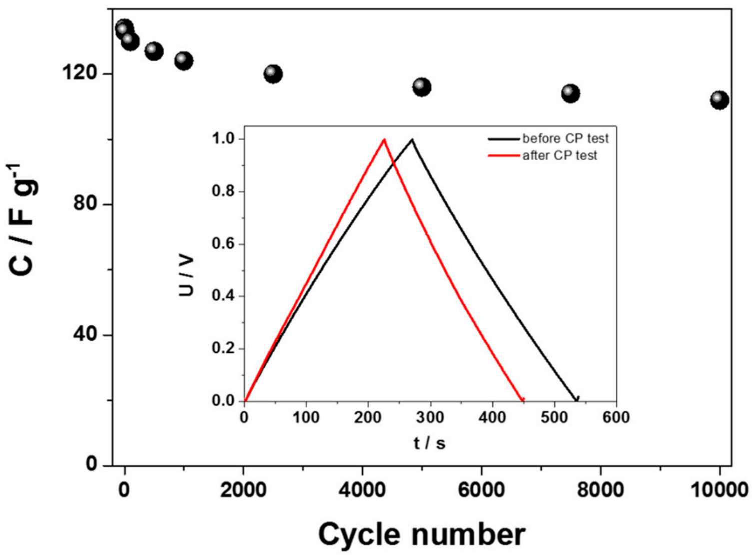

Figure 8. Curves of specific capacitance vs. cycle number for the hydrated non-crystalline WO_{3-x}. Inset: exemplary galvanostatic charge–discharge curves of electrodes at 0.5 A g^{-1} (in a two-electrode configuration).

The dependence of the specific capacitance of the hydrated WO_{3-x} electrode on the current density is shown in Figure 9a. The specific capacitance (C_s) was 122 A g^{-1} and 72 A g^{-1} at a current density of 0.5 A g^{-1} and 4 A g^{-1}, respectively. The capacitances were found to decrease by increasing the charge–discharge current. This is because, at a higher current density, the slower processes demonstrate a kinetic resistance and cannot participate in a charge transfer onto or across the electrode/electrolyte interface.

The Ragone plots display the relationship between the power density and energy density. In the case of the hydrated WO_{3-x}, at a power density of 803 W kg^{-1}, an energy density of 60 W h kg^{-1} was obtained. When the power density increased to 2520 W kg^{-1}, the energy density was 36 W h kg^{-1} (see Figure 9b), which is quite impressive as compared with earlier reports about modified metal oxides (Table S2) [32,33,35,66–74].

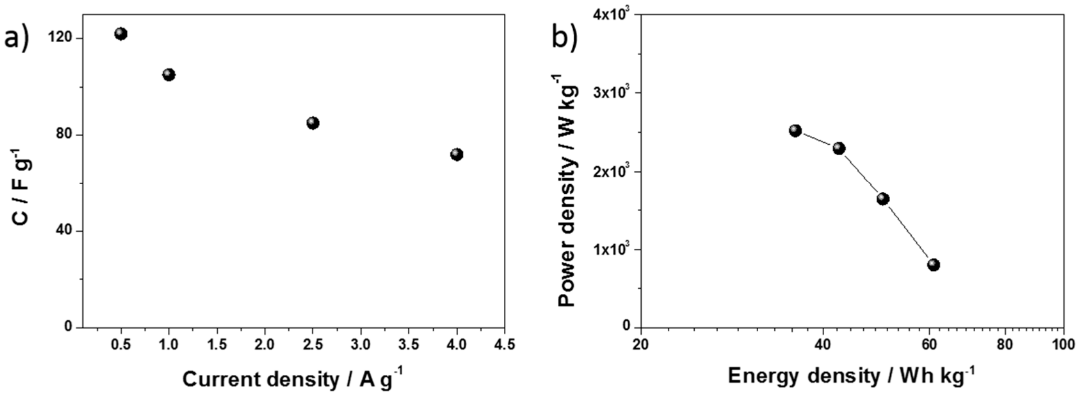

Figure 9. (**a**) Dependence of the specific capacitance of the hydrated WO_{3-x} electrode on the current density. (**b**) Ragone plot relating the energy and power densities of hydrated WO_{3-x} (in a two-electrode configuration).

3.2.2. Non-Aqueous Electrolyte

The electrochemical performances of the bulk and non-crystalline WO_3 electrode materials in a non-aqueous electrolyte are shown in Figure 10a. The first cyclic voltammetry curve for the bulk

WO_3 exhibits cathodic peaks corresponding to the lithium insertion into the WO_3 material (2.65 V and 2.37 V), according to the reaction below:

$$WO_3 + xLi^+ + xe^- \leftrightarrow Li_xW_x^{(V)}W^{(VI)}{}_{x-1}O_3 \text{ for } 0 \le x \le 1 \quad (3)$$

The cathodic maximum at 0.62 V might originate from a conversion reaction as shown below:

$$Li_xW_x^{(V)}W^{(VI)}{}_{x\text{-}1}O_3 + yLi^+ + ye^- \leftrightarrow W + 3\,Li_2O \text{ for } x + y = 6 \text{ and } 0 \le x \le 1 \quad (4)$$

Reaction (3) is similar to the reaction proposed for photointercalated molybdenum bronzes [75]. However, in the literature, one may find that WO_3 reacts with Li^+ and gives Li_xWO_3 [76,77], instead of $Li_xW_x^{(V)}W^{(VI)}{}_{x-1}O_3$.

During the oxidation process of the bulk WO_3, delithation occurs as a sharp anodic maximum at 1.25 V and a broad hump at 1.9 V. The former is attributed to the oxidation of W to $Li_xW_x^{(V)}W^{(VI)}{}_{x-1}O_3$, while the latter corresponds to the formation of WO_3. The cathodic maxima for the second cycle did not overlap with the cathodic maxima from the first cycle. In the second cycle there is no cathodic maximum at 0.62 V. The lack of a cathodic maximum at 0.62 V may suggest that the conversion reaction of a monoclinic WO_3 into $Li_xW_x^{(V)}W^{(VI)}{}_{x-1}O_3$ followed by the formation of a pure W is irreversible. This means that during the oxidation process, no monoclinic WO_3 is formed as a final product. There are three cathodic maxima at 1.67 V, 1.2 V and 0.15 V. The first two maxima may confirm the formation of $Li_xW_x^{(V)}W^{(VI)}{}_{x-1}O_3$, while the last maximum might be attributed to the lithium ion intercalation into carbon black, which is one of the components of the electrode material. The cyclic voltammetry curves of the oxidation process of the bulk WO_3 electrode material for the first and the second cycles are similar. One may see a broad anodic maximum at 1.3 V for both cycles. This maximum corresponds to the $Li_xW_x^{(V)}W^{(VI)}{}_{x-1}O_3$ oxidation with the WO_3 formation.

In the case of the non-crystalline WO_3, the shape of the first cyclic voltammetry curve differs from the shape of the first cyclic voltammetry curve originating from the bulk WO_3 electrode material. One may see broad humps with cathodic maxima at 2.2 V, 1.67 V, 1.45 V, 1.04 V and 0.25 V, with one wide anodic maximum at 1.41 V. The difference in shape may origin form the lack of a crystallographic order of the WO_3 nanoflakes. It is known that lithium ions intercalate into a WO_3 crystal framework and occupy trigonal cavity sites [77,78]. We assume that if there is no regular layer structure for the modified WO_3, lithium ions are not able to be inserted between the WO_3 layers. Thus, the specific capacity of the hydrated and non-crystalline WO_3 electrode material is much lower in comparison with the specific capacity of the bulk WO_3-based anode material (Figure 10b), unlike for the measurements in an aqueous electrolyte, where the charge storage ability is mainly influenced by the pseudocapacity of the surface groups.

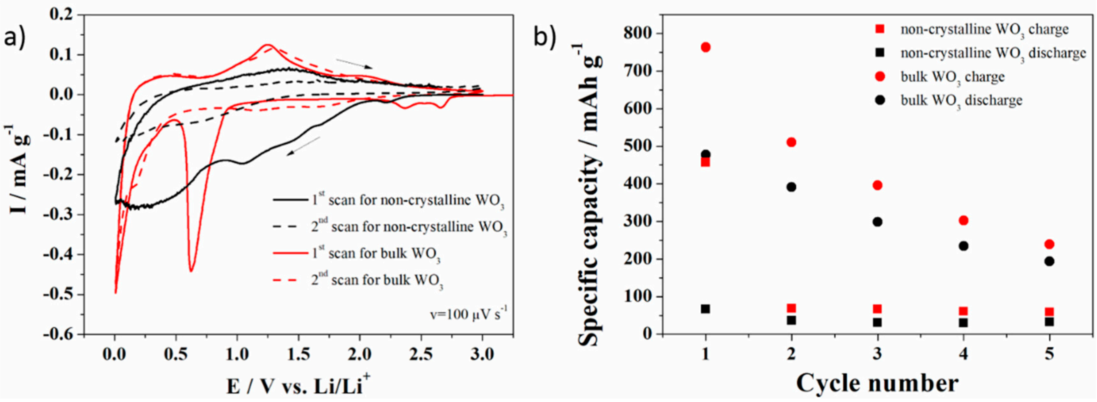

Figure 10. Electrochemical performance of the bulk and hydrated and non-crystalline WO_3 electrode material in 1 M $LiPF_6$ in EC/DMC 1:1 (**a**) cyclic voltammetry, (**b**) galvanostatic tests for battery application.

4. Conclusions

In the present work, the facile, eco-friendly water-based method is used to obtain hydrated and non-crystalline WO_{3-x}. This method is described in the literature as an exfoliation process, but in our case, we cannot clearly confirm that the exfoliated material was obtained. The developed strategy leads to the formation of nanoflakes of the hydrated and non-crystalline WO_3. Thus, it has been shown that the modified material is mainly amorphous, contains W(V) centers and is abundant with the surface groups. Bulk and non-crystalline WO_3 were tested as electrode materials in both an aqueous and non-aqueous electrolyte. Modified WO_3 exhibits a high specific pseudocapacitance due to the presence of surface groups, therefore, it can act as an efficient electrode material for supercapacitors. Multicyclic charge–discharge tests have confirmed the high electrochemical stability of the obtained material. On the other hand, a lack of crystallinity and a lack of a regularly layered structure do not allow the modified WO_3 to participate in the lithium ion intercalation, thus it cannot be used as an efficient electrode material for lithium-ion batteries.

Supplementary Materials: The following are available online at http://www.mdpi.com/1996-1944/13/8/1925/s1: Figure S1: SEM on higher magnification for hydrated WO_{3-x}, Figure S2: (a) CV curves of hydrated WO_{3-x} electrode in 0.2 M K_2SO_4. Scan rates 5–500 mV s^{-1}. Dependence of anodic current at 0.5 V (b) vs. scan rate and (c) vs. square root of the scan rate, Figure S3: The equivalent circuits used for modeling. Figure S4: The impedance spectra, experimental and fitted, of bulk WO_3 and hydrated WO_{3-x} recorded at 0 V and 0.6 V vs. Ag/AgCl (3 M KCl), Table S1: The results of fitting procedure, Table S2: Comparison of the electrochemical properties of the non-crystalline WO_3 with some previous reports on metal oxide-based supercapacitors.

Author Contributions: M.S.: Conceptualization, Investigation, Supervision, Writing—original draft preparation, Visualization, Writing–Review and Editing, Z.Z.: Validation, Writing—original draft preparation, Writing—Review and Editing, K.T.: Validation, Writing—original draft preparation, Writing—Review and Editing, G.T.: Investigation, A.P.N.: Investigation, Writing—original draft preparation, Writing—Review and Editing. All authors have read and agreed to the published version of the manuscript.

Funding: This research was funded by The National Centre for Research and Development via Grant No. LIDER/15/0088/L-10/18/NCBR/2019 (Integrated prototype of a photo-supercapacitor for energy storage obtained as a result of solar radiation conversion).

Conflicts of Interest: The authors declare no conflict of interest. The funders had no role in the design of the study; in the collection, analyses, or interpretation of data; in the writing of the manuscript, or in the decision to publish the results.

References

1. Lelieveld, J.; Klingmueller, K.; Pozzer, A.; Burnett, R.T.; Haines, A.; Ramanathan, V. Effects of fossil fuel and total anthropogenic emission removal on public health and climate. *Proc. Natl. Acad. Sci. USA* **2019**, *116*, 7192–7197. [CrossRef]
2. Murty, P. *Renewable Energy Sources*; Elsevier: Amsterdam, The Netherlands, 2017; pp. 783–800.
3. Sharma, P.; Bhatti, T. A review on electrochemical double-layer capacitors. *Energy Convers. Manag.* **2010**, *51*, 2901–2912. [CrossRef]
4. Woodbridge, J. Storage batteries. *J. Frankl. Inst.* **1924**, *198*, 271. [CrossRef]
5. Ujjain, S.K.; Singh, G.; Sharma, R.K. Co_3O_4@reduced graphene oxide nanoribbon for high performance asymmetric supercapacitor. *Electrochim. Acta* **2015**, *169*, 276–282. [CrossRef]
6. Szkoda, M.; Trzciński, K.; Rysz, J.; Gazda, M.; Siuzdak, K.; Lisowska-Oleksiak, A. Electrodes consisting of PEDOT modified by prussian blue analogues deposited onto titania nanotubes—Their highly improved capacitance. *Solid State Ion.* **2017**, *302*, 197–201. [CrossRef]
7. Ahuja, P.; Ujjain, S.K.; Kanojia, R. MnO x/C nanocomposite: An insight on high-performance supercapacitor and non-enzymatic hydrogen peroxide detection. *Appl. Surf. Sci.* **2017**, *404*, 197–205. [CrossRef]
8. Perna, P.; Maccariello, D.; Radovic, M.; Di Uccio, U.S.; Pallecchi, I.; Codda, M.; Marré, D.; Cantoni, C.; Gazquez, J.; Varela, M.; et al. Conducting interfaces between band insulating oxides: The $LaGaO_3/SrTiO_3$ heterostructure. *Appl. Phys. Lett.* **2010**, *97*, 152111. [CrossRef]
9. Rao, C.N.R.; Matte, H.S.S.R.; Maitra, U. Graphene analogues of inorganic layered materials. *Angew. Chem. Int. Ed.* **2013**, *52*, 13162–13185. [CrossRef] [PubMed]

10. Nicolosi, V.; Chhowalla, M.; Kanatzidis, M.G.; Strano, M.S.; Coleman, J.N. Liquid exfoliation of layered materials. *Science* **2013**, *340*, 1226419. [CrossRef]
11. Novoselov, K.; Geim, A.K.; Morozov, S.; Jiang, D.; Zhang, Y.; Dubonos, S.V.; Grigorieva, I.V.; Firsov, A.A. Electric field effect in atomically thin carbon films. *Science* **2004**, *306*, 666–669. [CrossRef] [PubMed]
12. Geim, A.K.; Grigorieva, I.V. Van der Waals heterostructures. *Nature* **2013**, *499*, 419–425. [CrossRef] [PubMed]
13. Guan, G.; Zhang, S.; Liu, S.; Cai, Y.; Low, M.; Teng, C.P.; Phang, I.Y.; Cheng, Y.; Duei, K.L.; Srinivasan, B.M.; et al. Protein induces layer-by-layer exfoliation of transition metal dichalcogenides. *J. Am. Chem. Soc.* **2015**, *137*, 6152–6155. [CrossRef] [PubMed]
14. Coleman, J.N.; Lotya, M.; O'Neill, A.; Bergin, S.D.; King, P.J.; Khan, U.; Young, K.; Gaucher, A.; De, S.; Smith, R.J.; et al. Two-dimensional nanosheets produced by liquid exfoliation of layered materials. *Science* **2011**, *331*, 568–571. [CrossRef] [PubMed]
15. Zhang, H. Ultrathin two-dimensional nanomaterials. *ACS Nano* **2015**, *9*, 9451–9469. [CrossRef]
16. Tang, C.-J.; He, J.; Jaing, C.-C.; Liang, C.-J.; Chou, C.-H.; Han, C.-Y.; Tien, C.-L. An all-solid-state electrochromic device based on WO_3–Nb_2O_5 composite films prepared by fast-alternating bipolar-pulsed reactive magnetron sputtering. *Coatings* **2018**, *9*, 9. [CrossRef]
17. Gao, H.; Yu, Q.; Chen, K.; Sun, P.; Liu, F.; Yan, X.; Liu, F.; Lu, G. Ultrasensitive gas sensor based on hollow tungsten trioxide-nickel oxide (WO3-NiO) nanoflowers for fast and selective xylene detection. *J. Colloid Interface Sci.* **2019**, *535*, 458–468. [CrossRef]
18. Hu, G.; Li, J.; Liu, P.; Zhu, X.; Li, X.; Ali, R.N.; Xiang, B. Enhanced electrocatalytic activity of WO_3@NPRGO composite in a hydrogen evolution reaction. *Appl. Surf. Sci.* **2019**, *463*, 275–282. [CrossRef]
19. Bi, Q.; Gao, Y.; Dang, C.; Wang, Z.; Xue, J.; Xue, J. Study on the photoelectrocatalytic performance of a WO_3 thin film electrode by constructing a BiOI/WO_3 heterojunction. *CrystEngComm* **2019**, *21*, 6744–6757. [CrossRef]
20. Qiu, M.; Shen, L.; Song, S.; Tan, S.; Sun, P.; Wang, K.; Yu, X.; Zhao, C.; Mai, W. WO3 nanoflowers with excellent pseudo-capacitive performance and the capacitance contribution analysis. *J. Mater. Chem. A* **2016**, *4*, 7266–7273. [CrossRef]
21. Mandal, D.; Routh, P.; Nandi, A.K. A new facile synthesis of tungsten oxide from tungsten disulfide: Structure dependent supercapacitor and negative differential resistance properties. *Small* **2017**, *14*, 1702881. [CrossRef]
22. Wang, P.; Cheng, Z.; Lv, G.; Qu, L.; Zhao, Y. Coupling interconnected MoO_3/WO_3 nanosheets with a graphene framework as a highly efficient anode for lithium-ion batteries. *Nanoscale* **2018**, *10*, 396–402. [CrossRef] [PubMed]
23. Lokhande, V.; Lokhande, A.; Namkoong, G.; Kim, J.H.; Ji, T. Charge storage in WO_3 polymorphs and their application as supercapacitor electrode material. *Results Phys.* **2019**, *12*, 2012–2020. [CrossRef]
24. Obregón, S.; Caballero, A.; Colón, G. Hydrothermal synthesis of $BiVO_4$: Structural and morphological influence on the photocatalytic activity. *Appl. Catal. B Environ.* **2012**, *117*, 59–66. [CrossRef]
25. Rahman, M.; MacElroy, J.M.D.; Dowling, D.P. Influence of the physical, structural and chemical properties on the photoresponse property of magnetron sputtered TiO_2 for the application of water splitting. *J. Nanosci. Nanotechnol.* **2011**, *11*, 8642–8651. [CrossRef]
26. Szubzda, B.; Szmaja, A.; Halama, A. Influence of structure and wettability of supercapacitor electrodes carbon materials on their electrochemical properties in water and organic solutions. *Electrochim. Acta* **2012**, *86*, 255–259. [CrossRef]
27. Nagy, D.; Szilágyi, I.M.; Fan, X. Effect of the morphology and phases of WO_3 nanocrystals on their photocatalytic efficiency. *RSC Adv.* **2016**, *6*, 33743–33754. [CrossRef]
28. Dutta, S.; Pal, S.; De, S. Mixed solvent exfoliated transition metal oxides nanosheets based flexible solid state supercapacitor devices endowed with high energy density. *New J. Chem.* **2019**, *43*, 12385–12395. [CrossRef]
29. Zhang, C.; Park, S.-H.; O'Brien, S.E.; Seral-Ascaso, A.; Liang, M.; Hanlon, D.; Krishnan, D.; Crossley, A.; McEvoy, N.; Coleman, J.N.; et al. Liquid exfoliation of interlayer spacing-tunable 2D vanadium oxide nanosheets: High capacity and rate handling Li-ion battery cathodes. *Nano Energy* **2017**, *39*, 151–161. [CrossRef]
30. Chang, K.-H.; Hu, C.-C. Oxidative synthesis of $RuO_x{\cdot}nH_2O$ with ideal capacitive characteristics for supercapacitors. *J. Electrochem. Soc.* **2004**, *151*, A958. [CrossRef]

31. Lu, X.; Yu, M.; Wang, G.; Zhai, T.; Xie, S.; Ling, Y.; Tong, Y.; Li, Y. H-TiO_2@MnO_2//H-TiO_2@C core-shell nanowires for high performance and flexible asymmetric supercapacitors. *Adv. Mater.* **2012**, *25*, 267–272. [CrossRef]
32. Luan, F.; Wang, G.; Ling, Y.; Lu, X.; Wang, H.; Tong, Y.; Liu, X.-X.; Li, Y. High energy density asymmetric supercapacitors with a nickel oxide nanoflake cathode and a 3D reduced graphene oxide anode. *Nanoscale* **2013**, *5*, 7984. [CrossRef] [PubMed]
33. Lu, X.; Zeng, Y.; Yu, M.; Zhai, T.; Liang, C.; Xie, S.; Balogun, M.-S.; Jie, T.; Tong, Y. Oxygen-deficient hematite nanorods as high-performance and novel negative electrodes for flexible asymmetric supercapacitors. *Adv. Mater.* **2014**, *26*, 3148–3155. [CrossRef] [PubMed]
34. Yang, P.; Xiao, X.; Li, Y.; Ding, Y.; Qiang, P.; Tan, X.; Mai, W.; Lin, Z.; Wu, W.; Li, T.; et al. Hydrogenated ZnO core-shell nanocables for flexible supercapacitors and self-powered systems. *ACS Nano* **2013**, *7*, 2617–2626. [CrossRef] [PubMed]
35. Zhai, T.; Xie, S.; Yu, M.; Fang, P.; Liang, C.; Lu, X.; Tong, Y. Oxygen vacancies enhancing capacitive properties of MnO2 nanorods for wearable asymmetric supercapacitors. *Nano Energy* **2014**, *8*, 255–263. [CrossRef]
36. Kim, H.; Cook, J.; Lin, H.; Ko, J.S.; Tolbert, S.H.; Ozolins, V.; Dunn, B.S. Oxygen vacancies enhance pseudocapacitive charge storage properties of MoO_{3-x}. *Nat. Mater.* **2016**, *16*, 454–460. [CrossRef]
37. Geim, A.K.; Novoselov, K.S. The rise of graphene. *Nat. Mater.* **2007**, *6*, 183–191. [CrossRef]
38. Smith, R.J.; King, P.J.; Lotya, M.; Wirtz, C.; Khan, U.; De, S.; O'Neill, A.; Duesberg, G.S.; Grunlan, J.C.; Moriarty, G.; et al. Large-scale exfoliation of inorganic layered compounds in aqueous surfactant solutions. *Adv. Mater.* **2011**, *23*, 3944–3948. [CrossRef]
39. Tagaya, H.; Ara, K.; Kadokawa, J.-I.; Karasu, M.; Chiba, K. Intercalation of organic compounds in the layered host lattice MoO_3. *J. Mater. Chem.* **1994**, *4*, 551. [CrossRef]
40. Murugan, A.V.; Viswanath, A.K.; Gopinath, C.S.; Vijayamohanan, K. Highly efficient organic-inorganic poly(3,4-ethylenedioxythiophene)-molybdenum trioxide nanocomposite electrodes for electrochemical supercapacitor. *J. Appl. Phys.* **2006**, *100*, 74319. [CrossRef]
41. Zhang, X.; Luo, Z.; Yu, P.; Cai, Y.; Du, Y.; Wu, D.; Gao, S.; Tan, C.; Li, Z.; Ren, M.; et al. Lithiation-induced amorphization of Pd3P2S8 for highly efficient hydrogen evolution. *Nat. Catal.* **2018**, *1*, 460–468. [CrossRef]
42. Shi, J.; Kuwahara, Y.; Wen, M.; Navlani-García, M.; Mori, K.; An, T.; Yamashita, H. Room-temperature and aqueous-phase synthesis of plasmonic molybdenum oxide nanoparticles for visible-light-enhanced hydrogen generation. *Chem. Asian J.* **2016**, *11*, 2377–2381. [CrossRef] [PubMed]
43. Wang, X.; Shi, W.; Jin, Z.; Huang, W.; Lin, J.; Ma, G.; Li, S.; Guo, L. Remarkable SERS activity observed from amorphous ZnO nanocages. *Angew. Chem. Int. Ed.* **2017**, *56*, 9851–9855. [CrossRef] [PubMed]
44. Peng, Z.; Jianping, L.; Yonghua, T.; Yuguang, C.; Fei, L.; Guo, S. Amorphous FeCoPOx nanowires coupled to g-C_3N_4 nanosheets with enhanced interfacial electronic transfer for boosting photocatalytic hydrogen production. *Appl. Catal. B Environ.* **2018**, *238*, 161–167. [CrossRef]
45. Meng, X.; Deng, D. Trash to treasure: Waste eggshells as chemical reactors for the synthesis of amorphous Co(OH)2 nanorod arrays on various substrates for applications in rechargeable alkaline batteries and electrocatalysis. *ACS Appl. Mater. Interfaces* **2017**, *9*, 5244–5253. [CrossRef] [PubMed]
46. Ren, Y.; Li, C.; Xu, Q.; Yan, J.; Li, Y.; Yuan, P.; Xia, H.; Niu, C.; Yang, X.; Jia, Y. Two-dimensional amorphous heterostructures of Ag/a-WO3- for high-efficiency photocatalytic performance. *Appl. Catal. B Environ.* **2019**, *245*, 648–655. [CrossRef]
47. Trzciński, K.; Szkoda, M.; Herman, A.; Borowska-Centkowska, A.; Lisowska-Oleksiak, A. Does the low optical band gap of yellow Bi_3YO_6 guarantee the photocatalytical activity under visible light illumination? *J. Solid State Electrochem.* **2018**, *22*, 2095–2105. [CrossRef]
48. Zhuiykov, S.; Kats, E. Enhanced electrical properties in sub-10-nm WO_3 nanoflakes prepared via a two-step sol-gel-exfoliation method. *Nanoscale Res. Lett.* **2014**, *9*, 401. [CrossRef]
49. Wei, Y.; Li, F.; Liu, L. Liquid exfoliation of Zn–Al layered double hydroxide using NaOH/urea aqueous solution at low temperature. *RSC Adv.* **2014**, *4*, 18044. [CrossRef]
50. Mehmood, F.; Iqbal, J.; Gul, A.; Ahmed, W.; Ismail, M. Facile synthesis of 2-D Cu doped WO_3 nanoplates with structural, optical and differential anti cancer characteristics. *Phys. E Low-Dimens. Syst. Nanostruct.* **2017**, *88*, 188–193. [CrossRef]

51. Etman, A.S.; Abdelhamid, H.N.; Yuan, Y.; Wang, L.; Zou, X.; Sun, J. Facile water-based strategy for synthesizing MoO_{3-x} nanosheets: Efficient visible light photocatalysts for dye degradation. *ACS Omega* **2018**, *3*, 2193–2201. [CrossRef]
52. Songara, S.; Gupta, V.; Patra, M.K.; Singh, J.; Saini, L.; Gowd, G.S.; Vadera, S.R.; Kumar, N. Tuning of crystal phase structure in hydrated WO_3 nanoparticles under wet chemical conditions and studies on their photochromic properties. *J. Phys. Chem. Solids* **2012**, *73*, 851–857. [CrossRef]
53. Kalantar-Zadeh, K.; Vijayaraghavan, A.; Ham, M.-H.; Zheng, H.; Breedon, M.; Strano, M.S. Synthesis of atomically thin WO_3 sheets from hydrated tungsten trioxide. *Chem. Mater.* **2010**, *22*, 5660–5666. [CrossRef]
54. Yan, J.; Wang, T.; Wu, G.; Dai, W.; Guan, N.; Li, L.; Gong, J. Tungsten oxide single crystal nanosheets for enhanced multichannel solar light harvesting. *Adv. Mater.* **2015**, *27*, 1580–1586. [CrossRef] [PubMed]
55. Waller, M.R.; Townsend, T.K.; Zhao, J.; Sabio, E.M.; Chamousis, R.L.; Browning, N.D.; Osterloh, F.E. Single-crystal tungsten oxide nanosheets: Photochemical water oxidation in the quantum confinement regime. *Chem. Mater.* **2012**, *24*, 698–704. [CrossRef]
56. Guan, G.; Xia, J.; Liu, S.; Cheng, Y.; Bai, S.; Tee, S.Y.; Zhang, Y.W.; Han, M. Electrostatic-driven exfoliation and hybridization of 2D nanomaterials. *Adv. Mater.* **2017**, *29*, 1700326. [CrossRef] [PubMed]
57. Liang, L.; Zhang, J.; Zhou, Y.; Xie, J.; Zhang, X.; Guan, M.; Pan, B.; Xie, Y. High-performance flexible electrochromic device based on facile semiconductor-to-metal transition realized by $WO_3{\cdot}2H_2O$ ultrathin nanosheets. *Sci. Rep.* **2013**, *3*, 1–8. [CrossRef] [PubMed]
58. Navío, C.; Vallejos, S.; Stoycheva, T.; Llobet, E.; Correig, X.; Snyders, R.; Blackman, C.; Umek, P.; Ke, X.; Van Tendeloo, G.; et al. Gold clusters on WO_3 nanoneedles grown via AACVD: XPS and TEM studies. *Mater. Chem. Phys.* **2012**, *134*, 809–813. [CrossRef]
59. Cárdenas, R.; Torres, J.; Alfonso, J. Optical characterization of MoO_3 thin films produced by continuous wave CO_2 laser-assisted evaporation. *Thin Solid Films* **2005**, *478*, 146–151. [CrossRef]
60. Li, Y.; Liu, Z.; Ruan, M.; Guo, Z.; Li, X. 1D WO_3 Nanorods/2D WO_{3-x} nanoflakes homojunction structure for enhanced charge separation and transfer towards efficient photoelectrochemical performance. *ChemSusChem* **2019**, *12*, 5282–5290. [CrossRef]
61. Li, S.; Yao, Z.; Zhou, J.; Zhang, R.; Shen, H. Fabrication and characterization of WO_3 thin films on silicon surface by thermal evaporation. *Mater. Lett.* **2017**, *195*, 213–216. [CrossRef]
62. Clatot, J.; Campet, G.; Zeinert, A.; Labrugere, C.; Nistor, M.; Rougier, A. Low temperature Si doped ZnO thin films for transparent conducting oxides. *Sol. Energy Mater. Sol. Cells* **2011**, *95*, 2357–2362. [CrossRef]
63. Luo, Z.; Poyraz, A.S.; Kuo, C.-H.; Miao, R.; Meng, Y.; Chen, S.-Y.; Jiang, T.; Wenos, C.; Suib, S.L. Crystalline mixed phase (anatase/rutile) mesoporous titanium dioxides for visible light photocatalytic activity. *Chem. Mater.* **2014**, *27*, 6–17. [CrossRef]
64. Shpak, A.; Korduban, A.; Medvedskij, M.; Kandyba, V. XPS studies of active elements surface of gas sensors based on WO_{3-x} nanoparticles. *J. Electron Spectrosc. Relat. Phenom.* **2007**, *156*, 172–175. [CrossRef]
65. Darmawi, S.; Burkhardt, S.; Leichtweiss, T.; Weber, D.A.; Wenzel, S.; Janek, J.; Elm, M.T.; Klar, P.J. Correlation of electrochromic properties and oxidation states in nanocrystalline tungsten trioxide. *Phys. Chem. Chem. Phys.* **2015**, *17*, 15903–15911. [CrossRef] [PubMed]
66. Xu, K.; Ma, S.; Shen, Y.; Ren, Q.; Yang, J.; Chen, X.; Hu, J.; Ren, R. $CuCo_2O_4$ nanowire arrays wrapped in metal oxide nanosheets as hierarchical multicomponent electrodes for supercapacitors. *Chem. Eng. J.* **2019**, *369*, 363–369. [CrossRef]
67. Raj, S.; Srivastava, S.K.; Kar, P.; Roy, P. In situ growth of Co_3O_4 nanoflakes on reduced graphene oxide-wrapped Ni-foam as high performance asymmetric supercapacitor. *Electrochim. Acta* **2019**, *302*, 327–337. [CrossRef]
68. Shinde, P.A.; Lokhande, A.C.; Chodankar, N.; Patil, A.M.; Kim, J.H.; Lokhande, C.D. Temperature dependent surface morphological modifications of hexagonal WO_3 thin films for high performance supercapacitor application. *Electrochim. Acta* **2017**, *224*, 397–404. [CrossRef]
69. Ramadoss, A.; Kim, S.-J. Improved activity of a graphene—TiO2 hybrid electrode in an electrochemical supercapacitor. *Carbon* **2013**, *63*, 434–445. [CrossRef]
70. Ahuja, P.; Ujjain, S.K.; Kanojia, R. Electrochemical behaviour of manganese & ruthenium mixed oxide@ reduced graphene oxide nanoribbon composite in symmetric and asymmetric supercapacitor. *Appl. Surf. Sci.* **2018**, *427*, 102–111. [CrossRef]

71. Du, D.; Lan, R.; Xu, W.; Beanland, R.; Wang, H.; Tao, S. Preparation of a hybrid $Cu_2O/CuMoO_4$ nanosheet electrode for high-performance asymmetric supercapacitors. *J. Mater. Chem. A* **2016**, *4*, 17749–17756. [CrossRef]
72. Gupta, S.P.; Patil, V.B.; Tarwal, N.L.; Bhame, S.D.; Gosavi, S.W.; Mulla, I.S.; Late, D.J.; Suryavanshi, S.S.; Walke, P. Enhanced energy density and stability of self-assembled cauliflower of Pd doped monoclinic WO_3 nanostructure supercapacitor. *Mater. Chem. Phys.* **2019**, *225*, 192–199. [CrossRef]
73. Nayak, A.K.; Das, A.K.; Pradhan, D. High performance solid-state asymmetric supercapacitor using green synthesized graphene—WO3 nanowires nanocomposite. *ACS Sustain. Chem. Eng.* **2017**, *5*, 10128–10138. [CrossRef]
74. Shinde, P.A.; Lokhande, V.C.; Patil, A.M.; Ji, T.; Lokhande, C.D. Single-step hydrothermal synthesis of WO_3-MnO_2 composite as an active material for all-solid-state flexible asymmetric supercapacitor. *Int. J. Hydrog. Energy* **2018**, *43*, 2869–2880. [CrossRef]
75. Szkoda, M.; Trzciński, K.; Klein, M.; Siuzdak, K.; Lisowska-Oleksiak, A. The influence of photointercalaction and photochromism effects on the photocatalytic properties of electrochemically obtained maze-like MoO_3 microstructures. *Sep. Purif. Technol.* **2018**, *197*, 382–387. [CrossRef]
76. Li, B.; Wang, Y.; Uchaker, E.; Pei, Y.; Cao, G.; Huang, B. Mesoporous tungsten trioxide polyaniline nanocomposite as an anode material for high-performance lithium-ion batteries. *ChemNanoMat* **2016**, *2*, 281–289. [CrossRef]
77. Pathak, R.; Gurung, A.; Elbohy, H.; Chen, K.; Reza, K.M.; Bahrami, B.; Mabrouk, S.; Ghimire, R.; Hummel, M.; Gua, Z.; et al. Self-recovery in Li-metal hybrid lithium-ion batteries via WO_3 reduction. *Nanoscale* **2018**, *10*, 15956–15966. [CrossRef] [PubMed]
78. Hibino, M.; Han, W.; Kudo, T. Electrochemical lithium intercalation into a hexagonal WO_3 framework and its structural change. *Solid State Ion.* **2000**, *135*, 61–69. [CrossRef]